ACS APPLIED OPTICAL MATERIALS

pubs.acs.org/acsaom

Article

Tunable Highly Efficient Photochromism and Multimodal Luminescence in $(Ca,Sr)_3MgSi_2O_8:Eu^{2+}$ Solid Solutions

Guna Krieke,* Andris Antuzevics, Guna Doke, Aivaras Kareiva, and Aleksej Zarkov

Cite This: *ACS Appl. Opt. Mater.* 2025, 3, 2173−2183

Read Online

ACCESS | Metrics & More | Article Recommendations | Supporting Information

ABSTRACT: Inorganic photochromic materials have been extensively studied for their potential applications in various fields such as anticounterfeiting, optical information storage, and smart windows. In this study, the tunable photochromic properties of $(Ca,Sr)_3MgSi_2O_8:Eu^{2+}$ compounds, which exhibit a composition-dependent photochromic effect varying from reddish-pink to yellow, are analyzed. All investigated materials exhibit excellent photochromic efficiency, ranging from 60% in $Sr_3MgSi_2O_8$ to 66−69% in $(Ca,Sr)_3MgSi_2O_8:Eu^{2+}$ solid solutions, reaching an unusually high value of 85% in $Ca_3MgSi_2O_8:Eu^{2+}$ − exceeding values reported for other currently known wide bandgap materials. Two dominant defect-related absorbance bands centered in the blue-green and near-infrared (NIR) spectral ranges are detected using diffuse reflectance spectroscopy (DRS). Thermostimulated luminescence (TSL) analysis reveals that the dominant TSL signal, with an activation energy of 1.45 eV, shows similar excitation and bleaching behavior to the photochromic effect and is likely associated with nonparamagnetic charge trap centers. Comparison of electron paramagnetic resonance (EPR) spectroscopy and DRS measurements indicates that the photochromism in $(Ca,Sr)_3MgSi_2O_8:Eu^{2+}$ is attributed primarily to the formation of F^+ centers, i.e., electrons trapped in oxygen vacancies, and suggests tunneling between defects. Among the investigated materials, $Ca_3MgSi_2O_8:Eu^{2+}$ demonstrates the best performance by combining superior color contrast, efficient optical and thermal stimulation, and unusually deep charge traps, making it a promising candidate for practical applications.

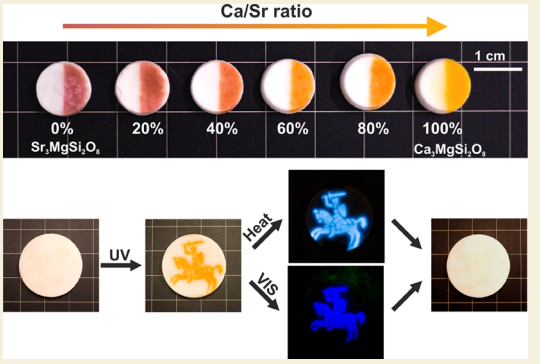

KEYWORDS: *photochromic effect, merwinite, Eu^{2+}, F^+ centers, color contrast*

1. INTRODUCTION

Photochromism, also called tenebrescence in minerals, is a reversible color change in a material upon exposure to light.[1,2] This phenomenon has been observed in both organic and inorganic materials, although the underlying mechanisms are different. In organic compounds, photochromism results from a light-induced transformation between two isomers with distinct absorption spectra.[3] In inorganic materials, the color changes can be related to redox processes, which have been analyzed in metal halides and transition metal oxides, or the light-induced trapping of electrons in charge traps, which is a commonly proposed mechanism in wide band gap materials.[4]

Compared to their organic counterparts, inorganic photochromic materials offer superior thermal, mechanical, and chemical properties, combined with a fast response to color changes and excellent cycling repeatability.[4] These advantages make them promising for a range of applications, such as anticounterfeiting and optical information storage,[5−7] optical thermometry,[8,9] dosimetry,[10,11] photocatalysis,[12,13] smart windows,[14] and self-erasing writings.[15,16] Notable inorganic photochromic materials include hackmanite $(Na_8Al_6Si_6O_{12}(Cl,S)_2)$,[2,17] $BaMgSiO_4$,[10,18] ferroelectric $K_{0.5}Na_{0.5}NbO_3$,[19,20] and transition metal oxides WO_3 and MoO_3, which have been widely studied for their efficient photochromic response.[21] A comprehensive overview of known inorganic photochromic materials has been provided in a recent review.[1]

Despite their promising properties, inorganic photochromic materials are currently overshadowed in practical applications by organic dyes and polymers.[22,23] Key challenges limiting their widespread use include typically low color contrast, limited color selection, and a lack of understanding of the fundamental mechanism of photochromic processes in most complex materials.[4] The color contrast can be improved by understanding the mechanism of the photochromic effect in the specific material and optimizing the synthesis conditions and dopants. The color, however, depends on the electronic properties of specific defects or color centers, which are characteristic of each host material. In wide-band gap materials,

Received: July 10, 2025
Revised: September 3, 2025
Accepted: September 4, 2025
Published: September 11, 2025

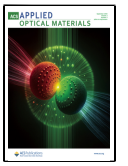

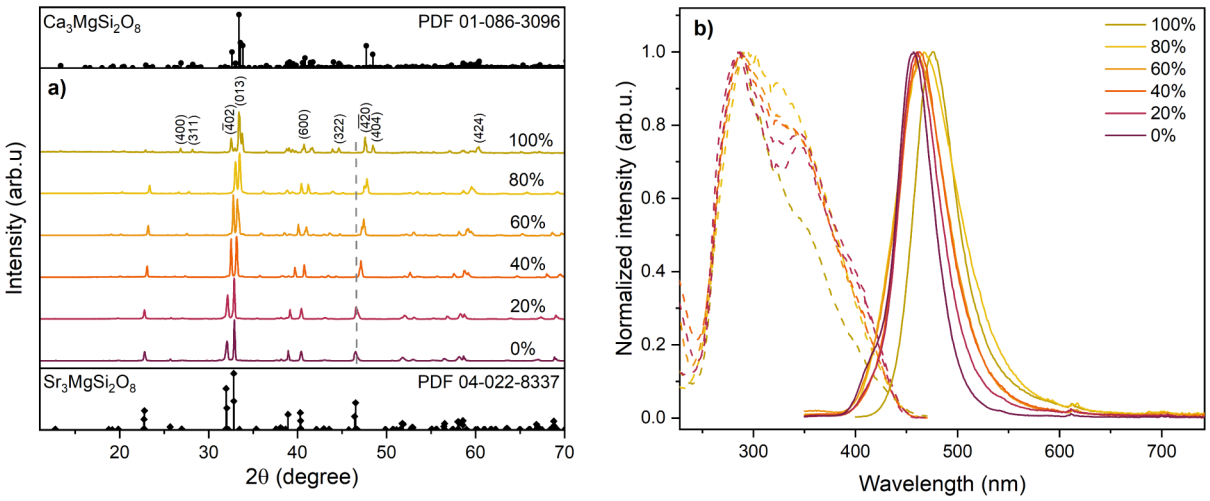

Figure 1. a) XRD patterns and the position of $(4\bar{2}0)$ plane of $Sr_3MgSi_2O_8$ marked with a dashed line and b) PLE (480 nm emission dashed lines) and PL (285 nm excitation, solid lines) spectra of Ca: 0−100% samples.

optical properties, including absorption band position, depend on the local environment of a specific center or defect. For instance, in alkali halides, the absorption of electrons trapped in halide vacancies (F-centers) is strongly influenced by cation−anion distances, with absorption peaks ranging from 244 nm in LiF to 727 nm in RbI.[24] A similar tunability has been reported in photochromic sodalites ($M_2(NaAlSiO_4)_6(X,Y,S_2)$, M = Li−Rb, X, Y = Cl−I), where variation in cation and anion composition resulted in a remarkable shift of F-center absorption bands from 438 to 682 nm.[25] These findings highlight the potential of crystal structure modification as a strategy for developing new photochromic materials with tunable optical properties.

Recent studies have identified efficient photochromic alkaline-earth silicates, $Ca_3MgSi_2O_8$ and $Sr_3MgSi_2O_8$.[16] These compounds form $Ca_3MgSi_2O_8$−$Sr_3MgSi_2O_8$ solid solutions,[26] which is a way to modify the crystal structure and the local environment of intrinsic defects. It was previously proposed that F^+-centers are one of the defects contributing to the photochromic effect of these materials.[16] The replacement of larger Sr^{2+} ions with smaller Ca^{2+} would reduce the interatomic distances in the $M_3MgSi_2O_8$ lattice. A subsequent shift in the absorption bands of F^+ centers can be expected.

In this study, we report tunable high-contrast photochromism varying from reddish-pink to yellow in $(Ca,Sr)_3MgSi_2O_8:Eu^{2+}$ solid solutions. The composition-dependent optical properties and the underlying photochromic mechanisms are analyzed in detail, providing new insights into the design of efficient photochromic materials.

2. RESULTS AND DISCUSSION

The crystal structure of $(Ca,Sr)_3MgSi_2O_8:Eu^{2+}$ was studied using X-ray diffraction (XRD) analysis. Diffraction patterns (Figure 1a) for $Ca_3MgSi_2O_8$ (Ca: 100%) and $Sr_3MgSi_2O_8$ (Ca: 0%) match well with their respective references—monoclinic $Ca_3MgSi_2O_8$ (PDF 01−086−3096) and monoclinic $Sr_3MgSi_2O_8$ (PDF 04-022-8337)—confirming phase purity. Both $Ca_3MgSi_2O_8$ and $Sr_3MgSi_2O_8$ crystallize in the monoclinic crystal structure with $P2_1/a$ space group. These compounds have three distinct Ca or Sr positions, one Mg position, two distinct Si positions, and eight distinct O positions.[26] The main structural difference between the two phases is the significantly smaller β angle of 90.0007° in $Sr_3MgSi_2O_8$,[26] in comparison to 91.9015° in $Ca_3MgSi_2O_8$,[27] which leads to noticeable peak overlap in the XRD pattern of $Sr_3MgSi_2O_8$. The low symmetry and presence of multiple distinct oxygen positions in the lattice may facilitate the formation of various oxygen-related defects.[28−30] This characteristic aligns with previous observations of multiple absorption bands in both photochromic $Ca_3MgSi_2O_8:Eu^{2+}$ and $Sr_3MgSi_2O_8:Eu^{2+}$.[16] Incorporation of Ca^{2+} into the $Sr_3MgSi_2O_8$ lattice resulted in a gradual shift of XRD peaks toward lower interplanar distances, highlighted with dashed lines for the $(4\bar{2}0)$ plane. This shift is associated with the replacement of larger Sr^{2+} ions (1.26 Å for 8-fold coordination) with smaller Ca^{2+} ions (1.12 Å for 8-fold coordination).[31] No additional phases were detected in the substituted samples, indicating the formation of a continuous $Ca_3MgSi_2O_8$−$Sr_3MgSi_2O_8$ solid solution with unlimited solubility.

Photoluminescence (PL) properties of the $(Ca,Sr)_3MgSi_2O_8:Eu^{2+}$ samples were analyzed using PL and photoluminescence excitation (PLE) measurements (Figure 1b). In all samples, the dominant excitation and emission signals are attributed to Eu^{2+} ions. The spectral positions of Ca: 0% and Ca: 100% closely match previously reported values for $Sr_3MgSi_2O_8:Eu^{2+}$ and $Ca_3MgSi_2O_8:Eu^{2+}$.[32,33] The PLE spectra of all investigated samples exhibit similar features, consisting of broad overlapping excitation bands with maxima at 285 and 344 nm, corresponding to the $4f^7 \rightarrow 4f^65d^1$ transitions of Eu^{2+}. In the PL spectra, the dominant broadband emission signals appear in the blue-green spectral range and are assigned to the $4f^65d^1 \rightarrow 4f^7$ transitions of Eu^{2+} ions. A gradual redshift in emission wavelength from 457 to 475 nm is observed with increasing Ca content. Previous extended X-ray absorption fine structure (EXAFS) analysis of $Ca_3MgSi_2O_8:Eu^{2+}$ and $Sr_3MgSi_2O_8:Eu^{2+}$ suggests that Eu^{2+} ions preferentially substitute into Ca/Sr sites with higher coordination numbers. In $Sr_3MgSi_2O_8$, Eu^{2+} is incorporated in Sr2 site, and in $Ca_3MgSi_2O_8$, Eu^{2+} can be reasonably modeled in either the Ca2 or Ca3 sites, which both give similar signals.[16] The shift in emission wavelength can be ascribed to both changes in the crystal field and incorporation of Eu^{2+} ions in multiple distinct Ca^{2+} and Sr^{2+} positions.[26]

https://doi.org/10.1021/acsaom.5c00275
ACS Appl. Opt. Mater. 2025, 3, 2173−2183

The observed red shift in the Eu^{2+} emission band with increasing Ca^{2+} content in $(Ca,Sr)_3MgSi_2O_8$ can be attributed to several interrelated factors. First, substitution of Sr^{2+} with the smaller Ca^{2+} ion reduces the average Eu−O bond length, resulting in a stronger crystal field that lowers the energy of the 5d excited state. Additionally, Ca^{2+} exhibits a slightly higher polarizing power compared to Sr^{2+}, leading to increased covalency in the Eu−O bonds. It reduces the energy of the 4f−5d transition and further contributes to the red shift. Similar results have been reported in other solid solutions.[34−36]

The DRS spectra of $(Ca,Sr)_3MgSi_2O_8:Eu^{2+}$ samples before and after UV irradiation (250 nm for 3 min) are shown in Figure 2a. Before irradiation, a relatively weak absorption signal is observed in the 320−450 nm range, corresponding to the $4f^7 \rightarrow 4f^65d^1$ transitions of Eu^{2+}. This absorption matches well with the PLE data presented in Figure 1b. After UV irradiation, multiple intense absorption bands appear in the visible range for all samples. In Ca: 0%, the dominant absorption bands are in the blue-green and red to NIR spectral regions with maxima located at 470 and 780 nm, leading to a reddish-pink coloration. As the Ca/Sr ratio increases, all absorption bands shift to shorter wavelengths, and the relative intensity of the NIR absorption band decreases. The results indicate that UV irradiation of $(Ca,Sr)_3MgSi_2O_8:Eu^{2+}$ causes the formation of at least two types of color centers with distinct absorption properties. Moreover, the two absorbance bands exhibit distinct thermal and time stability, discussed further in the text. Similar photochromic response has been previously reported in Eu^{2+} doped $Ca_3MgSi_2O_8$ and $Sr_3MgSi_2O_8$, which has been associated with the trapping of electrons in oxygen vacancies by forming F^+ centers.[16] The relative contribution to the overall spectrum and the spectral position of these centers are influenced by the Ca/Sr ratio, leading to composition-dependent color changes. As a result, a gradual shift in coloration from reddish-pink to yellow is observed (see Figure 2b).

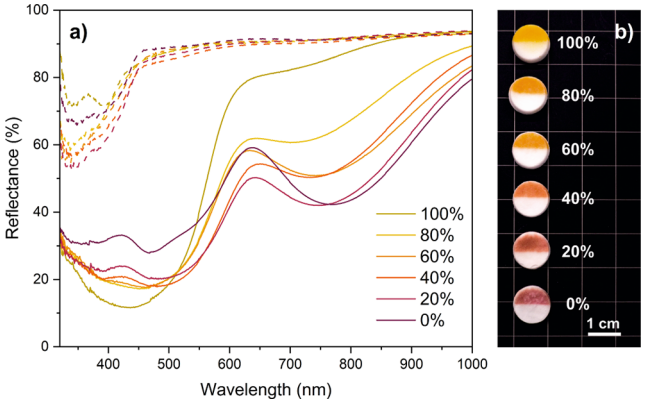

Figure 2. a) DRS spectra of Ca: 0−100% samples before (dashed lines) and after irradiation (solid lines) with 250 nm for 3 min; b) photograph of samples with the top half irradiated with 250 nm for 3 min.

The $(Ca,Sr)_3MgSi_2O_8:Eu^{2+}$ samples exhibit excellent color contrast, i.e., the difference in the absorbance before and after irradiation. The efficiency of photochromic materials can be calculated as the difference between the nonirradiated and irradiated states

$$\Delta R = R_0 - R_1 \quad (1)$$

where R_0 and R_1 are reflectance at a specific wavelength before and after irradiation, respectively.[37,38] In the investigated materials, ΔR of the most intense absorption bands in the green spectral range changes from 60% in $Sr_3MgSi_2O_8$ (Ca: 0%) to 66−69% in $(Ca,Sr)_3MgSi_2O_8:Eu^{2+}$ solid solutions, reaching a maximum of 72% in $Ca_3MgSi_2O_8$ (Ca: 100%). However, normalized intensity is more often reported:[1,39−42]

$$\Delta R_{norm} = \frac{R_0 - R_1}{R_0} \cdot 100 \quad (2)$$

The main advantage of eq 2 is that it can be adapted for other processes such as luminescence modulation and absorbance measurements in transparent materials. In the investigated materials, normalized photochromic efficiency ΔR_{norm} values for the maximum of absorbance bands in the blue spectral range increase from 68% in $Sr_3MgSi_2O_8$ (Ca: 0%) up to 85% in $Ca_3MgSi_2O_8$ (Ca: 100%), which is an

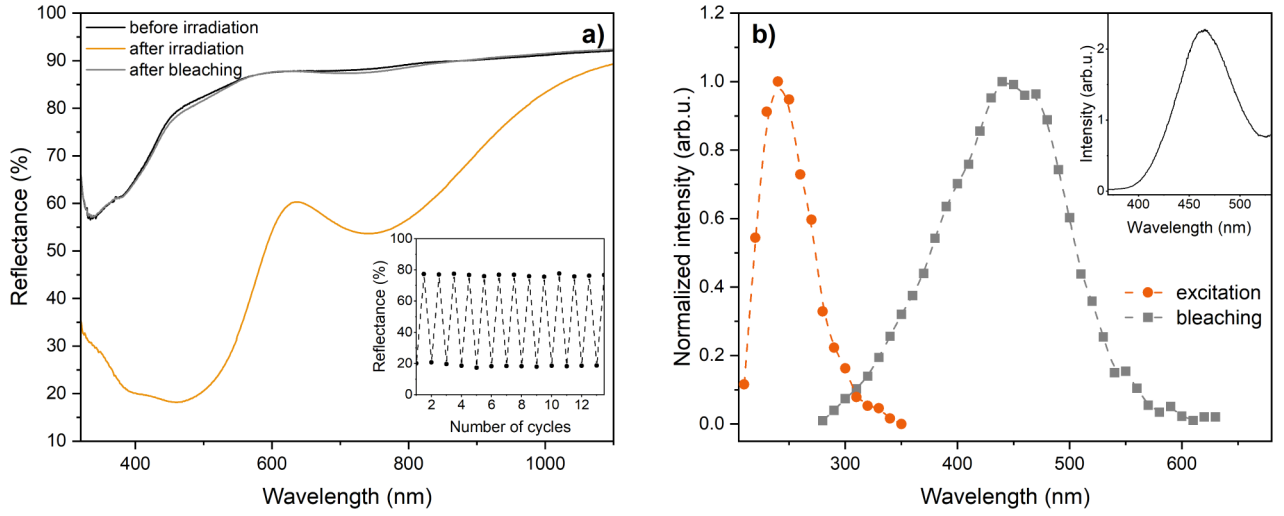

Figure 3. a) DRS spectra of Ca: 60% before irradiation, after irradiation with 250 nm for 3 min and after optical bleaching with 500 nm for 1 min (inset: reflectance at 450 nm after multiple irradiation and bleaching cycles); b) photochromic effect stimulation and bleaching spectra of Ca: 60% (inset: OSL spectrum detected during stimulation with 540 nm).

https://doi.org/10.1021/acsaom.5c00275
ACS Appl. Opt. Mater. 2025, 3, 2173−2183

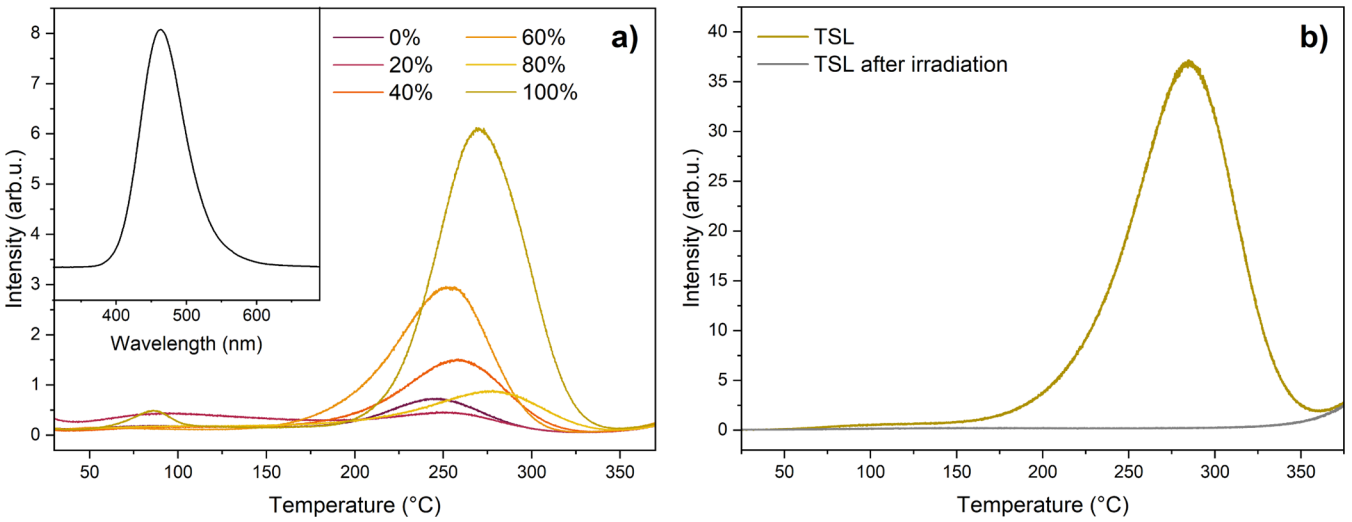

Figure 4. a) TSL glow curves of Ca: 0−100% samples and b) TSL glow curves of the Ca: 100% sample after irradiation with 263 nm and after irradiation with blue light (450 nm). Inset: TSL spectrum of Ca: 100% sample.

exceptionally high value that surpasses other wide band gap inorganic photochromic materials reported previously.[1] The results confirm that Eu^{2+} doped $Ca_3MgSi_2O_8$−$Sr_3MgSi_2O_8$ compounds, especially $Ca_3MgSi_2O_8$, are highly efficient photochromic materials. It should be noted that there is a significant overlap of absorbance bands and Eu^{2+} emission. As a result, a considerable decrease in the Eu^{2+} emission intensity can be detected after irradiation. To quantify this effect, PL measurements were performed on $(Ca,Sr)_3MgSi_2O_8$:Eu^{2+} samples excited at 420 nm before and after 250 nm irradiation for 3 min. In $Sr_3MgSi_2O_8$:Eu^{2+}, the integrated Eu^{2+} emission intensity under 420 nm excitation decreased by 87.3 ± 4.7% after irradiation. This decrease became progressively larger with increasing Ca content, from 89.3 ± 1.9% for Ca: 20% to 95.1 ± 0.3% for Ca: 80%, reaching a maximum of 96.6 ± 0.2% in $Ca_3MgSi_2O_8$:Eu^{2+}, which exhibits the strongest absorbance in the blue spectral range.

The color changes in the investigated materials are reversible and can be bleached thermally or using visible light. DRS spectra before irradiation, after irradiation, and after bleaching are shown in Figure 3a.

After bleaching, the reflectance spectra match well with spectra before irradiation, indicating that the samples can be reverted to the original state. No significant changes in the reflectance can be detected after multiple cycles of irradiation and bleaching. The results suggest that the color centers can be created repeatably even after multiple irradiations and bleaching cycles. Photochromic excitation and bleaching spectra of Ca: 60% are shown as an example in Figure 3b. The excitation spectrum shows a wide band located in the 200−300 nm range. Similar excitation spectra have been detected in Eu^{2+}-doped $Ca_3MgSi_2O_8$ and $Sr_3MgSi_2O_8$, reported previously,[16] therefore it is expected to be similar for all of the investigated $Ca_3MgSi_2O_8$−$Sr_3MgSi_2O_8$ samples. The bleaching or optical stimulation spectrum contains a broad band, located in the 350−550 nm range, with a maximum at 450 nm. The optical stimulation spectrum of Ca: 60% is in a similar spectral position as the dominant defect-related absorbance band in the blue-green spectral range, which suggests that during the excitation, defects related to this band are directly stimulated and liberated from charge traps. However, after the stimulation, both absorbance bands centered at 470 and 740 nm decrease in intensity (see Figure 3a), which can be associated with charge transfer processes between these two charge traps. The optical bleaching is accompanied by OSL (inset of Figure 3b). The OSL spectrum of Ca: 60% matches well with the Eu^{2+} emission shown in Figure 1b, suggesting that the recombination center in the OSL is likely Eu^{2+}.

In addition to the photochromic effect and OSL emission, TSL can be detected in all samples. To analyze the trap properties of the $(Ca,Sr)_3MgSi_2O_8$:Eu^{2+} samples, TSL glow curves were measured after irradiation with UV. The resulting TSL glow curves are shown in Figure 4a. The general structure of the glow curves is similar for all samples, with a low-intensity signal at temperatures below 170 °C and a dominant peak with a maximum in the 250−270 °C range. The highest TSL intensity and deepest charge traps were detected for Ca: 100%, which shows the potential of this material for dosimetry applications. It should be noted that consistently weaker TSL intensity of Ca: 80% sample compared with Ca: 100% and Ca: 60% has been observed. It may result from a combination of factors, including a lower charge trap concentration, reduced Eu^{2+} luminescence efficiency, or stronger overlap between Eu^{2+} emission and defect-related absorbance bands. Additionally, the TSL spectra of the samples were measured; the spectrum of Ca: 100% is shown in the inset of Figure 4a. The TSL spectra coincide with the PL spectra demonstrated in Figure 1b, thus ascribed to the Eu^{2+} luminescence. To compare the charge traps associated with defect-related optical properties, the TSL signal stability was evaluated after bleaching with blue light. It was observed that after exposure to a blue light LED, all charges were released from the defect centers, resulting in a complete bleaching of the TSL signal (see Figure 4b). The results indicate that the defects related to photochromic effect, OSL, and TSL can be optically bleached. The same defects are likely responsible for all three processes.

For an in-depth analysis, the Ca: 100% sample was selected. The T_{max}−T_{stop} method was employed to analyze the characteristics of traps by isolating individual glow peaks through incremental thermal cleaning, followed by the evaluation of activation energy via initial rise analysis (IRA), which assumes Arrhenius behavior in the low-temperature range of each peak. Both methods are well recognized and widely utilized.[43−45] A preheating step of 15 °C from 30 to 280

https://doi.org/10.1021/acsaom.5c00275
ACS Appl. Opt. Mater. 2025, 3, 2173−2183

°C was chosen, and for each measurement cycle, irradiation was carried out for 10 min. The obtained TSL glow curves and IRA plots are presented in Figure 5b,c. The calculated

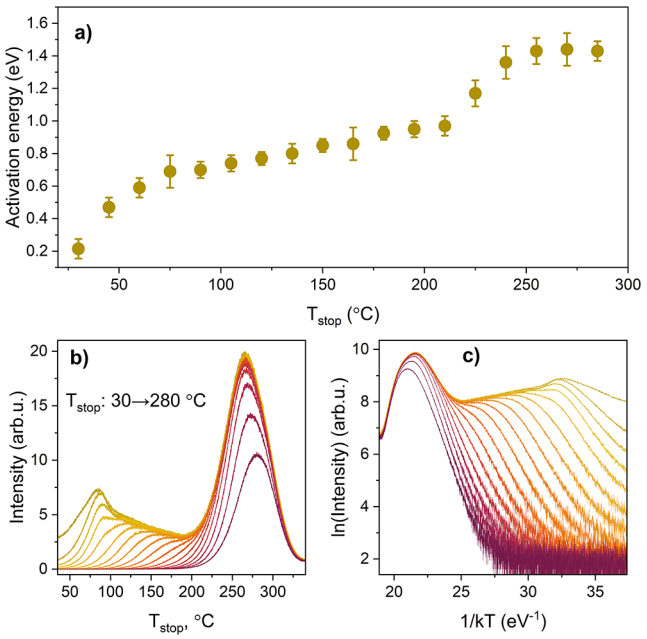

Figure 5. a) Activation energy values of the traps present in the Ca: 100% sample; b) $T_{max} - T_{stop;}$ and c) IRA plots of the same sample.

activation energies are depicted in Figure 5a. They can be classified into low and high energy ranges, with a threshold around 200 °C. The high-temperature glow peak can be characterized by an activation energy of about 1.45 eV. In contrast, the results for the low-temperature region are less conclusive; most activation energies fall within the 0.6−0.9 eV range. However, a trend of gradual increase in activation energy with higher T_{stop} indicates the presence of the same type of defects with slightly varying surroundings.

To identify the defects formed in $(Ca,Sr)_3MgSi_2O_8:Eu^{2+}$ solid solutions, EPR spectroscopy was used. After irradiation with UV (250 nm), EPR signals associated with paramagnetic centers emerge, consistent with previous investigations of the end members of $(Ca,Sr)_3MgSi_2O_8:Eu^{2+}$ solid solutions.[16] A comparison of the UV-generated signals is presented in Figure 6. Most samples, except for Ca: 100%, exhibit relatively broad, asymmetric peaks. The peak positions gradually shift toward higher magnetic field values with the increase of Sr content. The two low-intensity lines at ca. 355 mT observed in some of the samples originate from trace impurity ions.

Simulations of the UV-induced EPR signals were performed using the following spin-Hamiltonian (SH):

$$\hat{H} = \mu_B \vec{B} g \hat{S} + \hat{S} A \hat{I} \quad (3)$$

In eq 3, g is the g-factor; μ_B − the Bohr magneton; $\vec{B}$ − external magnetic field; $\hat{S}$ − electronic spin operator; A − HF coupling tensor; $\hat{I}$ − nuclear spin operator.[46] The HF interaction term was considered for the Ca: 100% sample only to explain the EPR spectrum structure in the 339−342 and 344−346 mT ranges. Experimentally, this signal was determined to increase with boron concentration (Figure S1). Both naturally occurring boron isotopes, ^{10}B (I = 3; natural abundance = 19.9%) and ^{11}B (I = 3/2; 80.1%), possess a magnetic moment. Multifrequency simulation results for the Ca: 100% and 0% samples are overviewed in Figure 7, while those for intermediary samples are shown in Figure S2. The determined SH parameters are provided in Table 1. Several points regarding the representation of simulation data should be noted: (1) Experimental spectra obtained after irradiation comprise multiple overlapping components with different stabilities. To simplify the simulations, the spectra recorded 1 day after irradiation were chosen for analysis. A tentative analysis of the unstable part is provided in Figure S3. (2) "C signal" refers to the group of signals observed in Ca-containing samples (Ca: 20−100%); note that HF structure was resolved in Ca: 100%. (3) Conversely, "S signal" refers to the signals identified in the Sr-containing samples (Ca: 0−80%). The

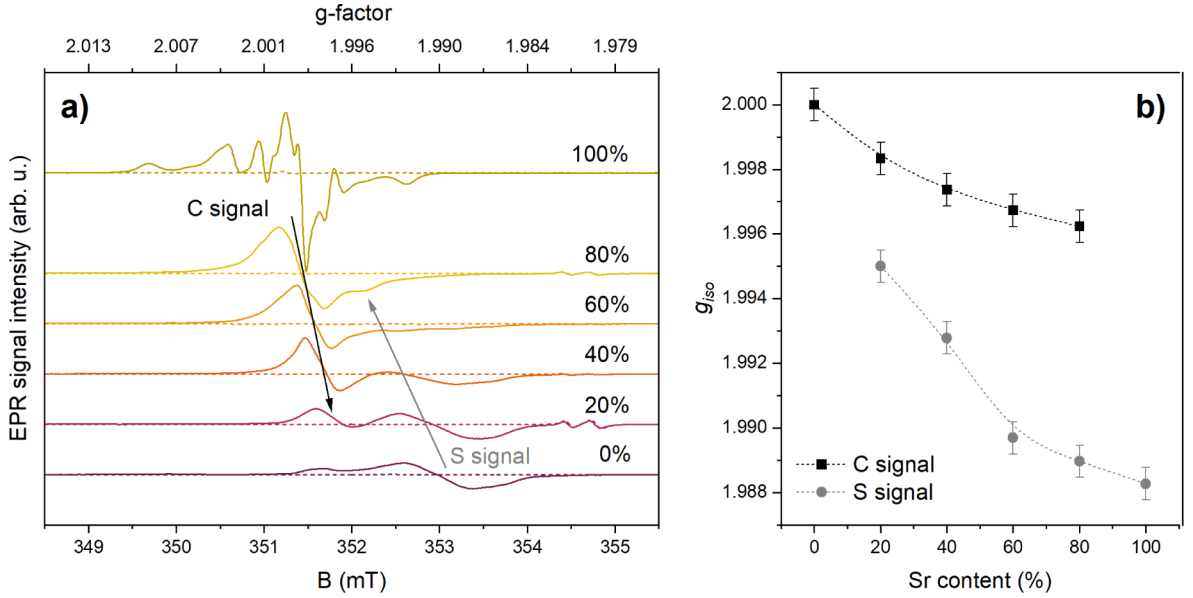

Figure 6. a) X-band EPR spectra of the Ca: 0−100% samples before (dashed lines) and after 250 nm irradiation for 3 min (solid lines). b) Variation of g_{iso} of the UV-generated paramagnetic centers with Sr content.

https://doi.org/10.1021/acsaom.5c00275
ACS Appl. Opt. Mater. 2025, 3, 2173−2183

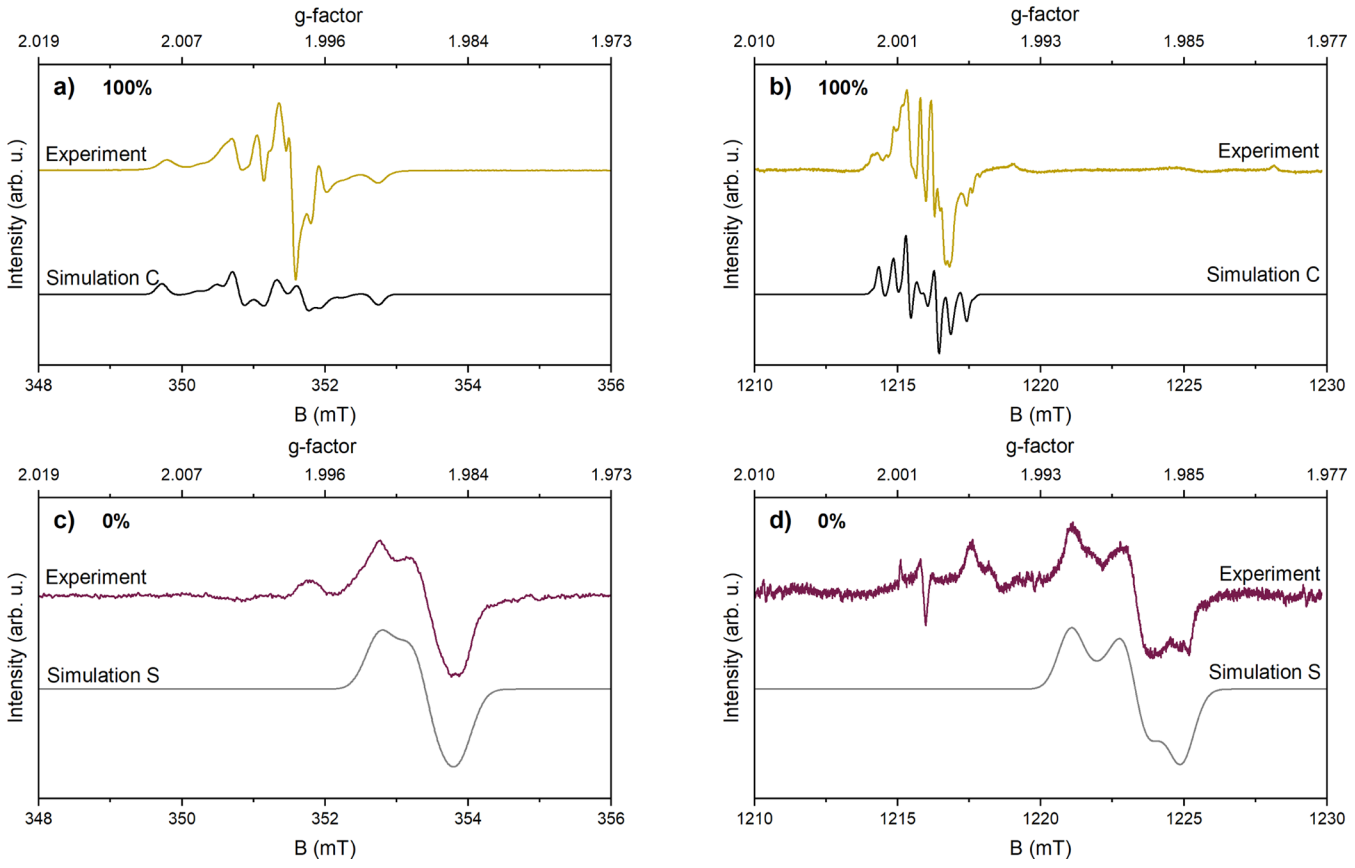

Figure 7. EPR spectra simulations of Ca: 100% ((a) X-band; (b) Q-band) and Ca: 0% ((c) X-band; (d) Q-band) samples after irradiation with 250 nm for 3 min.

Table 1. SH Parameters of the UV-Induced Paramagnetic Centers in the Investigated Samples

Sample	C signal				S signal			
	g_1	g_2	g_3	g_{iso}	g_1	g_2	g_3	g_{iso}
Ca: 100%	2.0006(10) A_1^{11B} = 11(3) MHz	2.0000(10) A_2^{11B} = 28(5) MHz	1.9994(10) A_3^{11B} = 10(3) MHz	2.0000				
Ca: 80%	1.9999(5)	1.9981(5)	1.9970(5)	1.9983	1.9950(5)	1.9950(5)	1.9950(5)	1.9950
Ca: 60%	1.9980(5)	1.9980(5)	1.9961(5)	1.9974	1.9938(5)	1.9938(5)	1.9908(5)	1.9928
Ca: 40%	1.9980(5)	1.9968(5)	1.9954(5)	1.9967	1.9931(5)	1.9897(5)	1.9863(5)	1.9897
Ca: 20%	1.9975(5)	1.9963(5)	1.9949(5)	1.9962	1.9922(5)	1.9887(5)	1.9856(5)	1.9890
Ca: 0%					1.9916(5)	1.9879(5)	1.9853(5)	1.9883

differentiation of multiple UV-generated EPR signals correlates with the formation of several color centers with distinct absorption properties.

The nature of UV-induced paramagnetic centers in $(Ca,Sr)_3MgSi_2O_8:Eu^{2+}$ can be discussed based on the simulation results. Both groups of EPR signals originate from $S = 1/2$ spin systems with rhombic symmetry g-factors ($g_1 \neq g_2 \neq g_3$). As the Sr content increases, the EPR resonance positions gradually shift to higher field values (Figure 6a), corresponding to decreasing g-factor values. This trend is illustrated in Figure 6. b by introducing $g_{iso} = (g_1 + g_2 + g_3)/3$. The results indicate two types of defects: one associated with single-phase $Ca_3MgSi_2O_8$ and the other with $Sr_3MgSi_2O_8$, both of which undergo gradual local structural transformations within the $(Ca,Sr)_3MgSi_2O_8$ solid solutions. This hypothesis is corroborated by the relative contributions of C and S signals depending on Ca and Sr content in Figure 6. Negative shifts from the free electron g-factor ($g_{iso} < g_e = 2.0023$) indicate that the UV-generated species are related to trapped electrons. The F^+ center – a single trapped electron at an oxygen vacancy – can be considered one of the primary $S = 1/2$ electron-type centers in oxides. Notably, the g_{iso} values determined for Ca: 100% and Ca: 0% here are close to those reported for F^+ centers in CaO ($g = 2.000$) and SrO ($g = 1.9845$),[47] respectively. Therefore, the formation of composition-dependent F^+-type centers involving native oxygen vacancy defects can be proposed in the $(Ca,Sr)_3MgSi_2O_8$ series upon exposure to UV radiation.

The time-dependent evolution of UV-induced EPR signals (Figure S3) reveals additional complexity in the investigated materials. Specifically, both the signal intensities and spectral shapes change over time. This observation implies that the experimental spectra are a superposition of multiple overlapping components with varying degrees of stability. The less stable components have been tentatively extracted as the simulation curves in Figure S3. Notably, the g-factor values of

https://doi.org/10.1021/acsaom.5c00275
ACS Appl. Opt. Mater. 2025, 3, 2173−2183

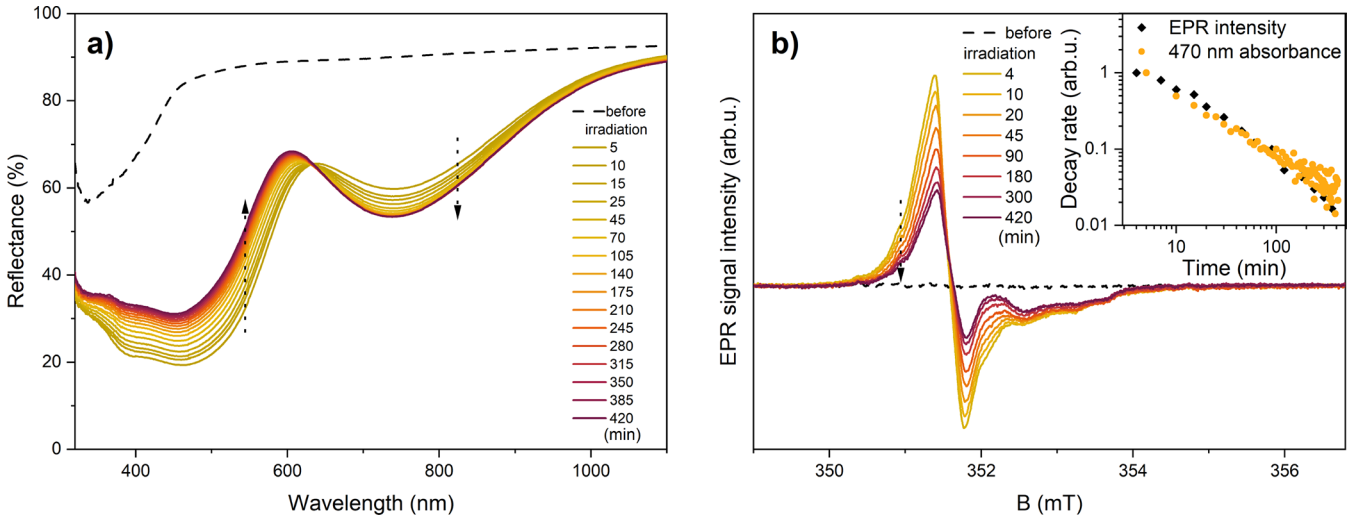

Figure 8. a) DRS spectra of Ca: 60% before (dashed lines) irradiation and 5−420 min after irradiation with 250 nm for 3 min; b) EPR spectra detected 4−420 min after irradiation with 250 nm. Inset: comparison of the decay rate of the 470 nm absorbance band and integral EPR intensity.

these unstable components are comparable to those of the relatively more stable ones listed in Table 1, which also suggests an association with F^+-type centers. The Ca: 100% sample provides an insightful example as EPR spectra HF structure is resolved for the stable component (Figure 7), while it is absent for the unstable component. It can be proposed that B^{3+} ions substituting Si^{4+} would generate a local positive charge deficiency, which is compensated by F^+-type centers. The absence of HF structure for the fast-decaying EPR signal in Ca: 100% suggests that such impurities are not located in the proximity of the paramagnetic center.

In summary, the EPR results demonstrate that UV-induced charge transfer processes generate F^+ type paramagnetic centers in $(Ca,Sr)_3MgSi_2O_8$ solid solutions. The two distinct F^+ signals are attributed to electrons trapped in different types of oxygen vacancies, likely located at two of the eight crystallographically distinct oxygen sites or influenced by local distortions from additives such as Eu or B, with distinct local environments. Each material contains multiple paramagnetic centers with varying degrees of stability. The local structure of these centers is influenced by the chemical composition of the host.

To understand the role of paramagnetic defects in the photochromism of the investigated materials, the time and temperature stabilities of EPR signals were compared with DRS data (see Figure 8a).

After prolonged storage in the dark, changes in the relative intensity of dominant absorbance bands were observed, indicating the thermal liberation of defects. A gradual decrease in the intensity of the dominant diffuse reflectance band with a maximum at 470 nm was detected. Interestingly, in parallel, an increase in the 740 nm band was observed. The results suggest a charge transfer process that leads to the formation of defects associated with the 740 nm band. Such effects were consistent across all samples, including Ca: 0% and Ca: 100%. Additionally, a decrease in the overall signal intensity was observed in the EPR spectra (Figure 8b). The decay rate of the 470 nm band closely matched the integral EPR signal (inset of Figure 8), indicating that 470 nm absorbance is related to paramagnetic F^+ centers. Similar results were obtained when comparing the thermal stability of DRS and EPR signals, shown in Figure 9a,b.

The intensity of the dominant absorbance band at 470 nm gradually decreased with increasing heat treatment temperature. Similar to time stability measurements, the intensity of the absorbance band at 740 nm gradually increased within the 25−125 °C range, followed by a decrease at higher temperatures. In the EPR spectra, a gradual decrease in the intensity of the C signal was detected (see Figure 9b), exhibiting thermal stability that matches the 470 nm band. The S signal, within the margin of error, correlates well with the 740 nm band. These results indicate that the dominant absorbance bands in the blue-green and red to NIR spectral ranges in $(Ca,Sr)_3MgSi_2O_8:Eu^{2+}$ are related to F^+ centers. However, the slightly higher thermal stability of the 470 nm band compared to the C signal indicates that this absorbance band likely consists of several overlapping bands associated with F^+ centers and nonparamagnetic color centers. The increase in intensity of the 740 nm band and the S signal could be attributed to tunneling of liberated electrons to vacancies with higher stability.

Similar to TSL, the activation energies for the decay of the photochromic signal and the EPR signal were evaluated using the Arrhenius equation as described elsewhere.[48,49] From DRS data, a trap depth of 0.22 ± 0.02 eV was obtained, while EPR measurements showed 0.19 ± 0.01 eV. The corresponding Arrhenius plots are shown in Figure S4. These low activation energies indicate that the associated F^+ centers are relatively unstable, and the 470 nm absorbance band is likely linked to TSL peaks occurring near room temperature. For the 740 nm band, higher activation energies were obtained: 0.55 ± 0.06 eV from DRS and 0.51 ± 0.03 eV from EPR. These values agree within experimental uncertainty; however, when compared to the TSL data, they are considerably lower than the activation energy of the dominant TSL peak. This dominant peak, with a maximum at 250−270 °C, can therefore be ascribed to nonparamagnetic charge traps of higher thermal stability than the paramagnetic F^+ centers and the defects responsible for the main absorbance bands. The results suggest that both paramagnetic and nonparamagnetic defects are formed in the investigated materials; however, the photochromic effect is mainly dominated by the formation of F^+ centers. The proposed mechanism of the photochromic effect with the excitation processes in $(Ca,Sr)_3MgSi_2O_8:Eu^{2+}$ is summarized in

https://doi.org/10.1021/acsaom.5c00275
ACS Appl. Opt. Mater. 2025, 3, 2173−2183

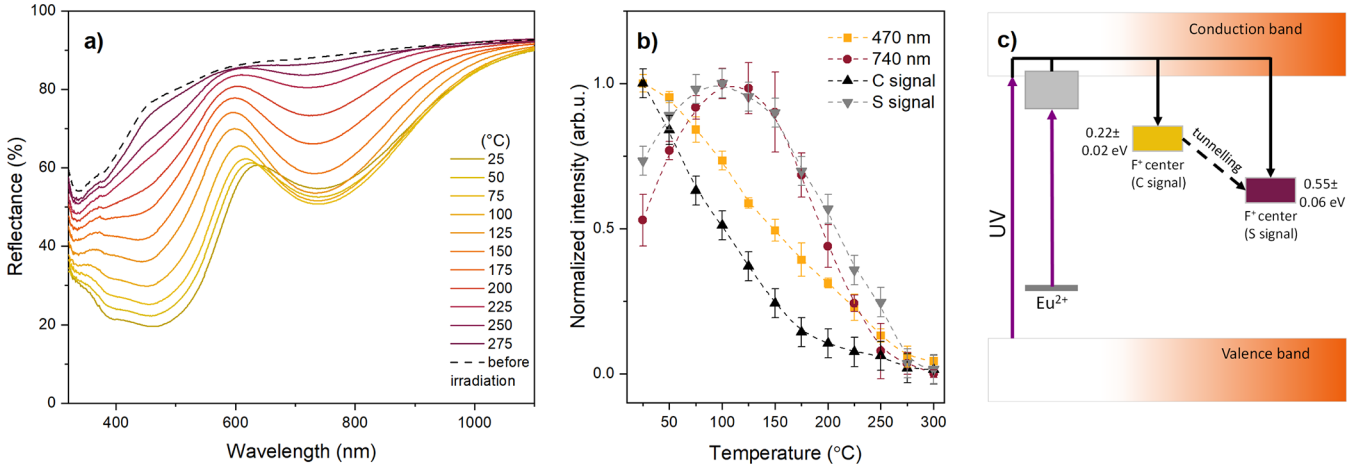

Figure 9. a) DRS spectra of Ca: 60% before (dashed lines) irradiation and after irradiation with 250 nm and heat treatment at 25−275 °C; b) Comparison of the thermal stability of the dominant absorbance band intensity with the C and S EPR signals; c) schematic representation of excitation process in $(Ca,Sr)_3MgSi_2O_8:Eu^{2+}$.

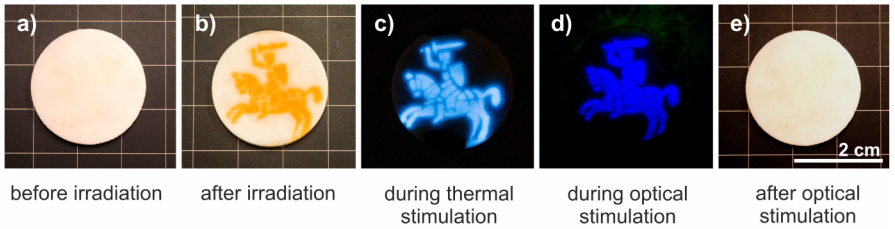

Figure 10. Photographs of Ca: 100% a) before irradiation; b) after irradiation with 250 nm for 1 min through photomask; c) during thermal stimulation at 250 °C; d) during optical stimulation with 532 nm (photograph taken through glass filter that attenuates green light); and e) after optical stimulation with 532 nm (analogous effect can be observed after thermal stimulation).

Figure 9c. During excitation, electrons are excited by UV light through band-to-band transitions or the photoionization of Eu^{2+} to Eu^{3+}, as confirmed previously.[16] The liberated charges are subsequently trapped in charge traps, which act as color centers. EPR and DRS analyses indicate that the dominant defects responsible for the main absorbance bands are electrons trapped in oxygen vacancies (F^+ centers); however, there is some contribution also from nonparamagnetic defects in the blue spectral range. The spectral positions of these bands depend on the chemical composition of the host. The replacement of Sr with Ca in $Sr_3MgSi_2O_8$ results in a gradual shift of the absorbance bands to higher energy, causing a color shift from reddish-pink to yellow.

Time and thermal stability measurements in Ca: 60% reveal that the defects related to the 470 nm band exhibit lower stability compared to the 740 nm band; therefore, we can expect that these defects are located closer to the conduction band. There is a charge transfer to the 740 nm band, resulting in an intensity increase after storage in darkness or heat treatment within the 25−125 °C range. The oxygen vacancies, forming F^+ centers, might be located near each other, allowing for quantum tunneling between them. The charges can be liberated from the traps either thermally, resulting in TSL, or optically, resulting in OSL. All defect-related absorbance bands can be fully bleached after both processes, demonstrating excellent reproducibility after multiple irradiation and bleaching cycles. The optical stimulation spectrum shown in Figure 3b matches well with the absorbance spectrum of the 470 nm band. However, both bands decrease in intensity during the stimulation. The quantum tunneling between the defects would result in both charge transfer between the vacancies and simultaneous depletion of the defects during the optical stimulation, therefore explaining the time and thermal stability as well as optical stimulation results.

$(Ca,Sr)_3MgSi_2O_8:Eu^{2+}$ compounds exhibit an unusually efficient photochromic effect and can be both thermally and optically stimulated. This combination of properties highlights the potential of these multimodal materials for practical applications. For instance, materials with multimodal optical properties have been extensively explored for anticounterfeiting, multimode imaging and information storage.[50−52] These studies, although centered on different mechanisms, underscore the potential of advanced materials in versatile optical systems. Furthermore, the integration of photochromic properties with TSL and OSL could enhance their functionality and security.[53−55] In this work, a ceramic plate of Ca: 100% was prepared and irradiated through a photomask. Photographs were taken in ambient light, as well as during thermal and optical stimulation (see Figure 10).

The design was clearly visible in both ambient light and during stimulation, and it could be erased afterward. The presence of deep charge traps, combined with the efficient photochromic effect, makes these materials promising for applications in dosimetry, anticounterfeiting, and rewritable optical storage.

3. CONCLUSIONS

The $(Ca,Sr)_3MgSi_2O_8:Eu^{2+}$ solid solutions exhibit a highly efficient and tunable photochromic effect, with the color shifting from reddish-pink to yellow as the Ca/Sr ratio

https://doi.org/10.1021/acsaom.5c00275
ACS Appl. Opt. Mater. 2025, 3, 2173−2183

increases. The incorporation of Ca^{2+}in the $Sr_3MgSi_2O_8:Eu^{2+}$ lattice improves the overall photochromic efficiency from 60% in $Sr_3MgSi_2O_8:Eu^{2+}$ to 66−69% in $(Ca,Sr)_3MgSi_2O_8:Eu^{2+}$ solid solutions reaching an outstanding level of 85% in $Ca_3MgSi_2O_8:Eu^{2+}$. To the best of our knowledge, this value surpasses the efficiency of all currently reported inorganic wide band gap materials. The photochromic effect in the investigated materials primarily originates from the trapping of electrons in oxygen vacancies, thus forming F^+ centers, although other nonparamagnetic defects also contribute to the absorbance band in the blue spectral range. The optical stimulation and defect stability experiments suggest that quantum tunneling between the defects formed after the irradiation likely contributes to the population and depopulation processes of charge traps. The combination of optically stimulated luminescence, deep charge trap centers, and efficient and reversible photochromic effect highlights the potential of these materials for practical applications in dosimetry, anticounterfeiting, and rewritable optical information storage

4. EXPERIMENTAL SECTION

4.1. Synthesis

High-purity precursors MgO (99.99%, Fisher Scientific), $CaCO_3$ (99.95%, Merck), $SrCO_3$ (99.997%, Fisher Scientific), SiO_2 (99.999%, Fisher Scientific), Eu_2O_3 (99.999%, Fisher Scientific), and H_3BO_3 (ACS Merck) were used for the synthesis. Samples with the general composition of $(Ca_{1-x}Sr_x)_3Mg_{1.1}Si_2O_8$: 0.01 mol % Eu^{2+} (x = 0−1) were prepared using the high-temperature solid-state reaction method. MgO was added in excess to prevent the formation of $(Ca,Sr)_2MgSi_2O_7$ as a secondary phase. 7.5 mol % H_3BO_3 was added as a flux by replacing the respective amount of SiO_2. The precursors were thoroughly mixed in an agate mortar and pressed into 13 mm pellets using a uniaxial hydraulic press from Specac. The pellets were annealed on graphite plates in a tube furnace HTRH 18/100/600 from Carbolite Gero at 1350 °C for 10 h in an H_2/Ar (5%/95%) atmosphere with a 5 °C/min heating and cooling rate. The samples are abbreviated as Ca y%, where y is a molar Ca percentage in $(Ca_{1-x}Sr_x)_3Mg_{1.1}Si_2O_8$ solid solution.

4.2. Characterization

The phase composition of the prepared samples was determined by XRD using a Rigaku MiniFlex 600 powder diffractometer (Cu Kα radiation, operated at 40 kV and 15 mA).

DRS spectra were measured using a double-beam spectrophotometer (Specord 210). To compare the DRS spectra of various samples and to perform EPR measurements, the samples were irradiated with 250 nm for 3 min using a wavelength-tunable laser (Ekspla NT342/3UV). After the irradiation, the samples were transferred to the spectrophotometer for measurement. Following each measurement, the samples were optically bleached with 500 nm for 1 min using a wavelength-tunable laser to reset the photochromic effect. The wavelength was selected to ensure bleaching and prevent the simultaneous excitation of Eu^{2+}. In the temperature stability experiments, samples were isostatically heated at specific temperatures for 2 min after the 250 nm irradiation. For the photochromic effect bleaching analysis, the samples were excited with 250 nm for 1 min, then bleached at a specific wavelength for 30 s.

PLE and PL spectra were measured using FLS1000 spectrometer from Edinburgh Instruments with a Xe lamp as an excitation source. The measured spectra were corrected to account for the wavelength-dependent response and resolution of the spectrometer system.

OSL spectra were measured using a wavelength-tunable laser Ekspla NT342/3UV as an excitation and optical stimulation source. The signal was detected using an Andor iSTAR DH734 CCD camera coupled to an Andor SR-303i-B spectrometer.

TSL glow curves and spectra were obtained using the Lexsyg research TSL/OSL reader from Freiberg Instruments GmbH. The signals were detected by a photomultiplier tube R13456 from Hamamatsu and a DV420A-BU2 CCD camera coupled to an Andor SR-303i-B spectrometer. For the irradiation source, a Q-switched short-pulsed UV laser (DTL-389QT) from the Laser-Compact Group, operating at a wavelength of 263 nm, was used. The samples were heated using a linear heating rate of 1 °C/s. To eliminate any effects from previously stored energy, the samples were preheated to 350 °C before each measurement. For blue light irradiation, built-in 450−460 nm LED operated at 100 mW was used.

The Bruker ELEXSYS-II E500 CW-EPR spectrometer was used for EPR investigations of the samples. The spectra acquisition settings were the following: room temperature, 9.832 GHz (X-band) or 34.03 GHz (Q-band) microwave frequency, 0.1 mW microwave power, and 0.1 mT magnetic field modulation amplitude. EPR signal intensities are normalized to 100 mg of sample mass. EPR spectra simulations were performed using the open-source MATLAB toolbox − EasySpin.[56]

For selective irradiation of samples, a polyvinyl chloride photomask was prepared using a laser engraver Nova 24 from Thunder Laser Europe.

■ ASSOCIATED CONTENT

Supporting Information

The Supporting Information is available free of charge at https://pubs.acs.org/doi/10.1021/acsaom.5c00275.

EPR characterization of samples, including signal evaluation with increasing boron content, spectra simulations, and signal stability; Arrhenius plots of photochromic absorbance and paramagnetic defects (PDF)

■ AUTHOR INFORMATION

Corresponding Author

Guna Krieke − *Institute of Chemistry, Vilnius University, Vilnius LT-03225, Lithuania; Institute of Solid State Physics, University of Latvia, Riga LV-1063, Latvia;* orcid.org/0000-0002-3561-1464; Email: guna.krieke@cfi.lu.lv

Authors

Andris Antuzevics − *Institute of Solid State Physics, University of Latvia, Riga LV-1063, Latvia;* orcid.org/0000-0001-7387-7207

Guna Doke − *Institute of Chemistry, Vilnius University, Vilnius LT-03225, Lithuania; Institute of Solid State Physics, University of Latvia, Riga LV-1063, Latvia;* orcid.org/0000-0003-4610-0974

Aivaras Kareiva − *Institute of Chemistry, Vilnius University, Vilnius LT-03225, Lithuania*

Aleksej Zarkov − *Institute of Chemistry, Vilnius University, Vilnius LT-03225, Lithuania;* orcid.org/0000-0002-3574-2296

Complete contact information is available at: https://pubs.acs.org/10.1021/acsaom.5c00275

Notes

The authors declare no competing financial interest.

■ ACKNOWLEDGMENTS

This project has received funding from the Research Council of Lithuania (LMTLT), Agreement No S-PD-24-67.

REFERENCES

(1) Li, D.; Zheng, X.; He, H.; Boutinaud, P.; Xiao, S.; Xu, J.; Wang, C.; Hu, Y.; Kang, F. A 20-Year Review of Inorganic Photochromic Materials: Design Consideration, Synthesis Methods, Classifications, Optical Properties, Mechanism Models, and Emerging Applications. *Laser Photonics Rev.* **2024**, *18* (11), 2400742.

(2) Medved, D. B. Hackmanite and Its Tenebrescent Properties. *Am. Mineral.* **1954**, *39*, 615−629.

(3) Zhang, J.; Zou, Q.; Tian, H. Photochromic Materials: More Than Meets The Eye. *Adv. Mater.* **2013**, *25* (3), 378−399.

(4) Du, J.; Yang, Z.; Lin, H.; Poelman, D. Inorganic Photochromic Materials: Recent Advances, Mechanism, and Emerging Applications. *Responsive Mater.* **2024**, *2* (2), No. e20240004.

(5) Hu, J.; Duan, B.; Yao, J.; Luo, T.; Wu, Y.; Wang, F.; Liu, T.; Ding, C.; Fan, Q.; Fu, H. Multimodal Anti-Counterfeiting and Optical Storage Application Based on Luminescence Reversible Modification and Color Change of Photochromic Phosphor. *Appl. Mater. Today* **2024**, *40*, 102392.

(6) Yu, F.; Wang, P.; Lin, J.; Zhou, P.; Ma, Y.; Wu, X.; Lin, C.; Zhao, C.; Gao, M.; Zhang, Q. $(K_{0.5}Na_{0.5})NbO_3$-Based Photochromic Transparent Ceramics for High-Security Dynamic Anti-Counterfeiting and Optical Storage Applications. *J. Lumin.* **2022**, *252*, 119345.

(7) Zhang, R.; Jin, Y.; Wang, C.; Chen, L.; Hu, Y. Photochromic Contrast Optimization Based on Hafmium-Based Ceramics for Optical Information Storage: Component Adjustment and Ion-Doping. *Ceram. Int.* **2023**, *49* (10), 15811−15817.

(8) Li, P.; Zhang, Z.; Xu, Z.; Sun, H.; Zhang, Q.; Hao, X. Photomodulated Cryogenic Temperature Sensing through a Photochromic Reaction in $Na_{0.5}Bi_{2.5}Ta_2O_9$: Er/Yb Multicolour Upconversion. *Opt. Express* **2023**, *31* (5), 7047.

(9) Li, X.; Guan, L.; Li, Y.; Sun, H.; Zhang, Q.; Hao, X. Optical Control of Er^{3+}-Doped $M_{0.5}Bi_{2.5}Nb_2O_9$. *J. Mater. Chem. C* **2020**, *8* (44), 15685−15696.

(10) Yang, Z.; Hu, J.; Van der Heggen, D.; Jiao, M.; Feng, A.; Vrielinck, H.; Smet, P. F.; Poelman, D. A Versatile Photochromic Dosimeter Enabling Detection of X-Ray, Ultraviolet, and Visible Photons. *Laser Photonics Rev.* **2023**, *17* (5), 2200809.

(11) Chen, H.; Xi, Z.; Guo, F.; Long, W.; Zhang, X.; Li, X.; Fang, P. Photochromic Ceramics for Multimode Detection of UV-VIS Radiation Dose. *Ceram. Int.* **2024**, *50* (3), 4885−4895.

(12) Zhou, F.; Ren, X. Reversible Photochromic Photocatalyst $Bi_2O_3/TiO_2/Al_2O_3$ with Enhanced Visible Photoactivity: Application toward UDMH Degradation in Wastewater. *J. Environ. Sci. Health Part A* **2020**, *55* (3), 239−255.

(13) Soares, L. G.; Alves, A. K. Photochromic Nanomaterials with Photocatalytic Application. In *Environmental Applications of Nanomaterials*; Springer: Cham, 2022; pp. 33−53.

(14) Meng, W.; Wang, J.; Jiang, L. Recent Advances in Photochromic Smart Windows Based on Inorganic Materials. *Responsive Mater.* **2024**, *2* (3), No. e20240001.

(15) Yang, Z.; Du, J.; Martin, L. I. D. J.; Van der Heggen, D.; Poelman, D. Highly Responsive Photochromic Ceramics for High-Contrast Rewritable Information Displays. *Laser Photonics Rev.* **2021**, *15* (4), 2000525.

(16) Krieke, G.; Antuzevics, A.; Kalinko, A.; Kuzmin, A.; Murauskas, T.; Kareiva, A.; Zarkov, A. Matrix-Dependent High-Contrast Photochromism in Eu-Doped $M_3MgSi_2O_8$ (M = Ca, Sr, Ba). *J. Mater. Chem. C* **2024**, *12* (41), 16989−16998.

(17) Norrbo, I.; Gluchowski, P.; Hyppänen, I.; Laihinen, T.; Laukkanen, P.; Mäkelä, J.; Mamedov, F.; Santos, H. S.; Sinkkonen, J.; Tuomisto, M.; Viinikanoja, A.; Lastusaari, M. Mechanisms of Tenebrescence and Persistent Luminescence in Synthetic Hackmanite $Na_8Al_6Si_6O_{24}(Cl,S)_2$. *ACS Appl. Mater. Interfaces* **2016**, *8* (18), 11592−11602.

(18) Akiyama, M.; Yamada, H.; Sakai, K. Multi Color Density Photochromism in Reduced Tridymite $BaMgSiO_4$ by Wavelength of Irradiation Light. *J. Ceram. Soc. Jpn.* **2011**, *119*, 105−109.

(19) Lin, J.; Wang, P.; Wang, H.; Shi, Y.; Zhu, K.; Yan, F.; Li, G.; Ye, H.; Zhai, J.; Wu, X. Significantly Photo-Thermochromic KNN-Based "Smart Window" for Sustainable Optical Data Storage and Anti-Counterfeiting. *Adv. Opt. Mater.* **2021**, *9* (17), 2100580.

(20) Yu, F.; Chi, Y.; Wang, P.; Ma, B.; Wu, X.; Lin, C.; Zhao, C.; Gao, M.; Lin, T.; Zhang, Q. Highly Responsive Photochromic Behavior with Large Coloration Contrast in Ba/Sm Co-Doped $(K_{0.5}Na_{0.5})NbO_3$ Transparent Ceramics. *Ceram. Int.* **2022**, *48* (13), 18899−18908.

(21) Bin Ahmad Kayani, A.; Kuriakose, S.; Khalid, F. A.; Bhaskaran, M.; Sriram, S.; Walia, S.; Monshipouri, M.; Monshipouri, M.; Abdul Khalid, F.; Walia, S.; et al. UV Photochromism in Transition Metal Oxides and Hybrid Materials. *Small* **2021**, *17* (32), 2100621.

(22) Towns, A. D. *Industrial Photochromism*; Springer: Cham, 2016; pp. 227−279. DOI: .

(23) Zou, J.; Liao, J.; He, Y.; Zhang, T.; Xiao, Y.; Wang, H.; Shen, M.; Yu, T.; Huang, W. Recent Development of Photochromic Polymer Systems: Mechanism, Materials, and Applications. *Research* **2024**, *7*, 0392.

(24) Popov, A. I.; Kotomin, E. A.; Maier, J. Basic Properties of the F-Type Centers in Halides, Oxides and Perovskites. *Nucl. Instrum. Methods Phys. Res., Sect. B* **2010**, *268* (19), 3084−3089.

(25) Byron, H. C.; Swain, C.; Paturi, P.; Colinet, P.; Rullan, R.; Halava, V.; Le Bahers, T.; Lastusaari, M. Highly Tuneable Photochromic Sodalites for Dosimetry, Security Marking and Imaging. *Adv. Funct. Mater.* **2023**, *33* (42), 2303398.

(26) Yonesaki, Y.; Takei, T.; Kumada, N.; Kinomura, N. Crystal Structure of Eu^{2+}-Doped $M_3MgSi_2O_8$ (M: Ba, Sr, Ca) Compounds and Their Emission Properties. *J. Solid State Chem.* **2009**, *182* (3), 547−554.

(27) Moore, P. B.; Araki, T. Atomic Arrangement of Merwinite, $Ca_3Mg[SiO_4]_2$, an Unusual Dense-Packed Structure of Geophysical Interest. *Am. Mineral.* **1972**, *57*, 1355−1374.

(28) Laguta, V. V.; Nikl, M.; Vedda, A.; Mihokova, E.; Rosa, J.; Blazek, K. Hole and Electron Traps in the $YAlO_3$ Single Crystal Scintillator. *Phys. Rev. B* **2009**, *80* (4), 045114.

(29) Gonzales-Lorenzo, C. D.; Gundu Rao, T. K.; Ccollque-Quispe, A. A.; Ayala-Arenas, J.; Gomes, M. B.; Silva-Carrera, B. N.; Gennari, R. F.; Pachas, V. S.; Monzon-Macedo, F.; Loro, H.; Chubaci, J. F. D.; Cano, N. F.; Rocca, R. R.; Watanabe, S. Study of the Centers Responsible for the TL Emission by EPR and PL Analysis of Eu-Doped $CaSiO_3$ Phosphors Synthesized by the Devitrification Method. *Mater. Res. Bull.* **2024**, *171*, 112607.

(30) Singh, N.; Singh, V.; Watanabe, S.; Chubaci, J. F. D.; Rao, T. K. G.; Gao, H.; Mardina, P. Studies of Defects and Optical Properties of $CaAl_{12}O_{19}$: Ho^{3+}. *Phosphor Material. J. Alloys Compd.* **2016**, *663*, 235−242.

(31) Shannon, R. D.; Prewitt, C. T. Revised Values of Effective Ionic Radii. *Acta Crystallogr., Sect. B* **1970**, *26* (7), 1046−1048.

(32) Lin, Y.; Tang, Z.; Zhang, Z.; Nan, C. W. Luminescence of Eu^{2+} and Dy^{3+} Activated $R_3MgSi_2O_8$-Based (R = Ca, Sr, Ba) Phosphors. *J. Alloys Compd.* **2003**, *348* (1−2), 76−79.

(33) Lee, C. Y.; Wu, C. C.; Li, H. H.; Yang, C. F. Synthesis and Luminescence Properties of Eu^{2+}-Doped $Sr_3MgSi_2O_8$ Blue Light-Emitting Phosphor for Application in Near-Ultraviolet Excitable White Light-Emitting Diodes. *Nanomaterials* **2022**, *12* (15), 2706.

(34) Wang, Z.; Wang, Y.; Zhang, P.; Fan, X.; Qian, G. Tunable Afterglow Color in Eu^{2+} and Dy^{3+} Co-Activated Alkaline Earth Feldspar Solid Solutions Phosphors. *J. Lumin.* **2007**, *124* (1), 140−142.

(35) Wang, Z.; Xia, Z.; Molokeev, M. S.; Atuchin, V. V.; Liu, Q. Blue-Shift of Eu^{2+} Emission in $(Ba,Sr)_3Lu(PO_4)_3$: Eu^{2+} Eulytite Solid-Solution Phosphors Resulting from Release of Neighbouring-Cation-Induced Stress. *Dalton Trans.* **2014**, *43* (44), 16800−16804.

(36) Leanenia, M. S.; Lutsenko, E. V.; Rzheutski, M. V.; Pavlovskii, V. N.; Yablonskii, G. P.; Naghiyev, T. G.; Tagiev, B. G.; Abushev, S. A.; Tagiev, O. B. Photoluminescence of $Ca_xBa_{1-x}Ga_2S_4$: Eu^{2+} Solid Solutions in Wide Excitation Intensity and Temperature Intervals. *J. Lumin.* **2017**, *181*, 121−127.

(37) Gong, J.; Du, P.; Li, W.; Yuan, G.; Mao, X.; Luo, L. The Enhancement of Photochromism and Luminescence Modulation

https://doi.org/10.1021/acsaom.5c00275
ACS Appl. Opt. Mater. 2025, 3, 2173−2183

Properties of Ferroelectric Ceramics via Chemical and Physical Strategies. *Laser Photonics Rev.* **2022**, *16* (10), 2200170.
(38) Yang, Z.; Du, J.; Martin, L. I. D. J.; Feng, A.; Cosaert, E.; Zhao, B.; Liu, W.; Van Deun, R.; Vrielinck, H.; Poelman, D. Designing Photochromic Materials with Large Luminescence Modulation and Strong Photochromic Efficiency for Dual-Mode Rewritable Optical Storage. *Adv. Opt. Mater.* **2021**, *9* (20), 2100669.
(39) Liu, M.; Shao, J.; Li, X.; Guo, Y.; Lu, C.; Ke, S.; Sun, H.; Zhang, Q. $BaMgSiO_4$-Based Composites with Photochromic and Persistent Luminescent Behaviors for Advanced Anti-Counterfeiting Applications. *Ceram. Int.* **2025**, *51* (16), 21735−21741.
(40) Tang, W.; Zuo, C.; Ma, C.; Wang, Y.; Li, Y.; Yuan, X.; Wang, E.; Wen, Z.; Cao, Y. Designing Photochromic Materials with High Photochromic Contrast and Large Luminescence Modulation for Hand-Rewritable Information Displays and Dual-Mode Optical Storage. *Chem. Eng. J.* **2022**, *435*, 134670.
(41) Zuo, C.; Tang, W.; Ma, C.; Chang, C.; Fan, K.; Li, Y.; Yuan, X.; Wen, Z.; Cao, Y. $BaMg_{0.28}Zr_{0.16}Ta_{0.56}O_3$: Dy^{3+} an Reversible Inorganic Photochromic Material with Large Photochromic Efficiency and High Luminescence Modulation. *J. Lumin.* **2023**, *255*, 119585.
(42) Wan, J.; Xu, J.; Zhu, S.; Li, J.; Ying, G.; Chen, K. Photochromic Composites with Fast Light Response, High Contrast, and Waterproof Properties. *J. Cleaner Prod.* **2023**, *419*, 138281.
(43) McKeever, S. W. S. On the Analysis of Complex Thermoluminescence. Glow-Curves: Resolution into Individual Peaks. *Phys. Status Solidi A* **1980**, *62* (1), 331−340.
(44) McKeever, S. W. S. *Thermoluminescence of Solids*; Cambridge University Press, 1985; Vol. 3.
(45) Bos, A. J. J. Theory of Thermoluminescence. *Radiat. Meas.* **2006**, *41*, S45−S56.
(46) Weil, J. A.; Bolton, J. R. *Electron Paramagnetic Resonance*; Wiley, 2007.
(47) Hughes, A. E.; Henderson, B. Color Centers in Simple Oxides. In *Point defects in solids*; Springer: Boston, 1972; pp. 381−490.
(48) Toyoda, S.; Ikeya, M. Thermal Basis Stabilities of Paramagnetic Defect and Impurity Centers in Quartz: For ESR Dating of Thermal History. *Geochem. J.* **1991**, *25*, 437.
(49) Bensimon, Y.; Deroide, B.; Dijoux, F.; Martineau, M. Nature and Thermal Stability of Paramagnetic Defects in Natural Clay: A Study by Electron Spin Resonance. *J. Phys. Chem. Solids* **2000**, *61* (10), 1623−1632.
(50) Kuang, Q.; Hou, X.; Du, C.; Wang, X.; Gao, D. Recent Advances in the Anti-Counterfeiting Applications of Long Persistent Phosphors. *Phys. Chem. Chem. Phys.* **2023**, *25* (27), 17759−17768.
(51) Gao, D.; Gao, F.; Kuang, Q.; Zhang, X.; Zhang, Z.; Pan, Y.; Chai, R.; Jiao, H. Zinc Germanate Nanophosphors with Persistent Luminescence for Multi-Mode Imaging of Latent Fingerprints. *ACS Appl. Nano Mater.* **2022**, *5* (7), 9929−9939.
(52) Jia, C.; Gao, D.; Wang, Z.; Zhang, X.; Yun, S.; Zhang, J. Z.; Wang, X. Tailoring Traps in Eu^{2+} Activated Persistent Phosphors for Multilevel Information Storage and Encryption. *Mater. Today Chem.* **2024**, *39*, 102182.
(53) Hu, Y.; Gao, D.; Zhang, X.; Yun, S. Controllable Thermo-Stimulated Luminescence in Niobate Persistent Phosphor by Constructing the Photovoltaic/Electrolytic Cell for Remote Intelligent Anti-Counterfeiting. *Chem. Eng. J.* **2025**, *509*, 161181.
(54) Zhang, X.; Wang, Z.; Xu, C.; Gao, D.; Pang, Q.; Xu, J.; Wang, X. Advanced Intelligent Anti-Counterfeiting in a Memory Storage Phosphor Through Response of Charge Carriers to Temperature. *Laser Photonics Rev.* **2025**, *19* (4), 2401376.
(55) Gao, D.; Du, C.; Wang, Y.; Xu, W.; Gao, W.; Pang, Q.; Wang, Y. Controllable Persistent Luminescence in Bismuth Activated Memory Phosphors by Trap Management for Artificial Intelligence Anti-Counterfeiting. *J. Mater. Chem. C* **2024**, *12* (48), 19487−19497.
(56) Stoll, S.; Schweiger, A. EasySpin, a Comprehensive Software Package for Spectral Simulation and Analysis in EPR. *J. Magn. Reson.* **2006**, *178* (1), 42−55.

https://doi.org/10.1021/acsaom.5c00275
ACS Appl. Opt. Mater. 2025, 3, 2173−2183